**Noris Gallandat**
Mem. ASME
Department of Mechanical Engineering,
The George W. Woodruff School
of Mechanical Engineering,
Georgia Institute of Technology,
Atlanta, GA 30332

**Federico Bonetto**
School of Mathematics,
Georgia Institute of Technology,
Atlanta, GA 30332

**J. Rhett Mayor**
Mem. ASME
Department of Mechanical Engineering,
The George W. Woodruff School
of Mechanical Engineering,
Georgia Institute of Technology,
Atlanta, GA 30332
e-mail: rhett.mayor@me.gatech.edu

# Ionic Wind Heat Transfer Enhancement in Vertical Rectangular Channels: Experimental Study and Model Validation

*This paper presents the results of an experimental study of ionic wind heat transfer enhancement in internal rectangular channels. Ionic wind is a potential technique to enhance natural convection cooling noise-free and without using moving part and thus ensuring a high reliability and a long lifetime. The goal of the present study is twofold: first, the multiphysics numerical model of ionic wind developed in previous work is validated experimentally. Second, the potential of the heat sink concept combining a fin array with an ionic wind generator is demonstrated by building a technology demonstrator. The heat sink presented in this work dissipates 240 W on a baseplate geometry of $200 \times 263$ mm. It is shown that the baseplate temperature can be reduced from $100\,^{\circ}C$ under natural convection to $81\,^{\circ}C$ when the ionic wind generator is turned on.*
[DOI: 10.1115/1.4035291]

## Introduction

The advent of novel electronic components exhibiting ever increasing computing power combined with a constant miniaturization trend has posed new challenges in terms of thermal management. Natural air convection—which is traditionally preferred in the field of electronics cooling for its simplicity and lack of hazard—is now being pushed to its limits [1]. In order to be able to benefit of the advantages of natural air convection cooling, new airflow enhancement techniques need to be developed.

Ionic wind has emerged as a potential candidate to enhance natural convection in heat transfer applications [2,3]. It is especially attractive for applications requiring high levels of reliability that prevent the use of any moving parts, for instance, power electronics meant to be part of the electricity distribution grid or systems part. Additionally, it operates nearly noise-free, which is an advantage as compared to pumps or fans.

**Ionic Wind Heat Transfer Enhancement.** Ionic wind generation occurs in two subsequent steps: First, ions are produced by a sharp electrode—e.g., a needle or a thin wire—that is maintained at a high voltage (in the order of several kilovolts). Then, ions travel from the high voltage electrode to a grounded electrode positioned downstream of the flow path. Momentum is transferred to the fluid through collision between the ions and the neutral air molecules, thereby inducing an air flow. The effect achieved is similar to the effect of a fan, but for the fact that momentum is transferred to the medium through collision of ions instead of the angular momentum transfer across the propeller blade.

The first step—the actual ion generation—is a very complex physical phenomenon that includes dozens of electronic reactions. Several studies have attempted to model the Corona discharge numerically [4–6]. However, the high complexity and the computational burden associated with such methods make it inappropriate as a design tool for the development of new heat sinks.

Therefore, the present approach suggests a hybrid method combining the experimental characterization of the Corona current with a numerical procedure to determine the flow- and heat-transfer enhancement caused by ionic wind. The numerical model describing flow- and heat-transfer enhancement through ionic wind was presented in previous work by Gallandat and Mayor [7] and is shortly summarized here. It is mentioned that Figs. 7–13 in Ref. [7] are incorrect due to an index error in the numerical procedure, which was corrected in a subsequently published errata [8].

The phenomenon of ionic wind heat transfer enhancement is governed by a set of five partial differential equations. The electric field is described by the Poisson equation (1). The charge density $\rho_e$ is the sum of the free electrons and positive and negative ions concentration multiplied by the elementary charge, as shown in Eq. (2). In the case of a positive Corona discharge considered in this work, the number of negative ions and free electrons outside the plasma region is several orders of magnitude smaller than the number of positive ions, as shown by Junhong and Davidson [9]. Therefore, the domain outside of the plasma region is considered unipolar, and the concentration of free electrons and negative ions is assumed to be zero. The permittivity of air takes a value of $\varepsilon = 8.859 \times 10^{-12}$ F/m. The next partial differential equation imposes conservation of charges. Free charges are transported by four mechanisms: conduction, drift, advection, and mass diffusion. Typically, the dominant ion transport mechanism is drift due to the electric field [3,10,11]. The thermofluidic part of the problem is described by the steady-state conservation equations for mass (4), momentum (5), and energy (6). The influence of ions on the fluid flow enters the conservation of momentum equation in the form of an electrostatic force proportional to the ion density and the electric field, the last term in Eq. (5). To fully describe the conservation of energy, the heat generated by the electrical current in the medium should be taken into account [11]. This is done by adding a Joule heating term—the second to last term in Eq. (6). The last term in Eq. (6) subtracts the kinetic energy that ions transfer to the fluid, as part of the ion energy is not converted to heat

$$\bar{\nabla} \cdot \bar{E} = -\nabla^2 \Phi = \frac{\rho_e}{\varepsilon} \qquad (1)$$
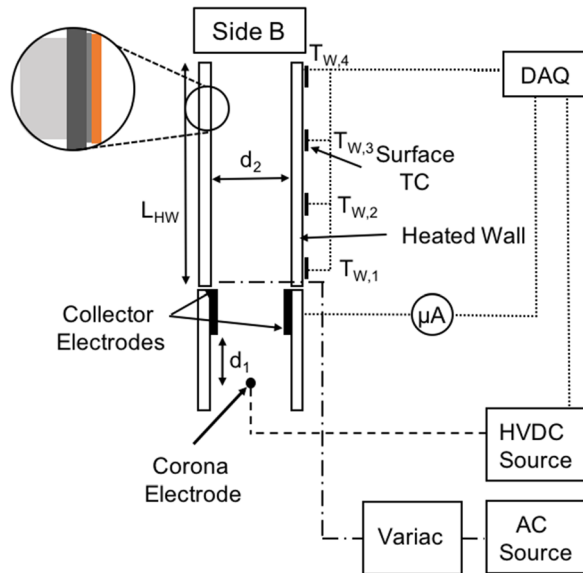
**Fig. 1   Sketch of the thermal test setup**



**Fig. 2   Moveable stand for the air velocity sensor allowing to collect data points across the channel**

$$\rho_e = (n_+ - n_- - n_e) \cdot e \tag{2}$$

$$\bar{\nabla} \cdot (\sigma\bar{E} + b\bar{E}\rho_e + \bar{u}\rho_e) = D_{\mathrm{IA}}\nabla^2\rho_e \tag{3}$$

$$\bar{\nabla} \cdot (\rho\bar{u}) = 0 \tag{4}$$

$$\bar{\nabla} \cdot (\rho\bar{u}\bar{u}) = -\bar{\nabla}p + \nu\nabla^2\bar{u} + \rho\bar{g} + \rho_e\bar{E} \tag{5}$$

$$\bar{u} \cdot \bar{\nabla}(\rho c_p T) = k\nabla^2 T + b\rho_e E^2 - \bar{u} \cdot (\rho_e\bar{E}) \tag{6}$$

The authors developed a numerical procedure to solve this set of five partial differential equations in previous work [7]. The objectives of the present paper are twofold. On the one hand, experimental data are collected in order to validate the numerical model presented above. On the other hand, a technology demonstrator is built to demonstrate the potential and the applicability of the presented technology.

The validation is performed at two levels: first, the velocity at the exit of the ionic wind generator is measured and compared to the model prediction. Second, a thermal test is conducted on a single cooling channel. The predicted heat rate is compared to the measured value for the cooling power.

## Experimental Setup

The ionic wind thermal test setup consists of an ionic wind generator and a heated channel. The test setup should allow for modularity so that both air velocity measurements and thermal data can be collected. A schematic of the thermal test setup is shown in Fig. 1. The e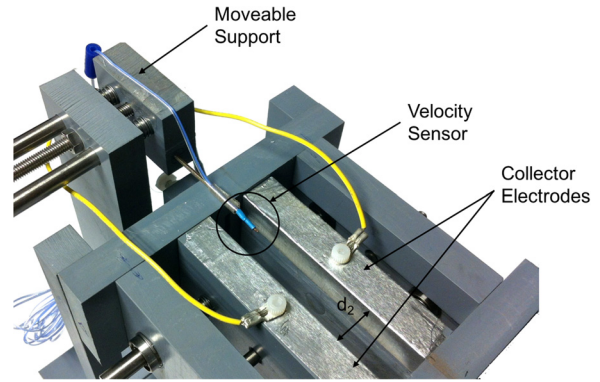quipment used as well as the uncertainty of the measurement apparatus are summarized in Table 1. The high voltage is provided by a high voltage DC source (Spellman CZE1000R), and the Corona current is measured using a picoammeter (Keithley Model 480).

The air velocity measurement presents two challenges: first, the expected velocity magnitudes are relatively low (in the order of 1–2 m/s). Second, the width of the channel is 20 mm or less. Therefore, a small velocity sensor is required in order to measure the velocity profile across the channel width. The microprofile airflow sensor UAS2000 developed by Degree Controls (Milford, NH) has a size of less than 1 mm and allows for velocity measurements in the range of 0.50–10 m/s. Therefore, this device proved to be the ideal tool for the present application. The velocity sensor is mounted at the exit of the ionic wind generator on a moveable stand in order to record the velocity profile across the width of the channel, as presented in Fig. 2.

The structure of the cooling channel is made of chlorinated polyvinyl chloride (CPVC). The advantage of CPVC is that it is an electrical insulator and therefore prevents any short circuit or unwanted Corona discharge. Further, it is easily machinable and has a maximum operating temperature of 95 °C, which is higher than conventional PVC and fulfills the requirements for the thermal testing to be performed. The parts are first water-jet cut and then finished on a three-axis computer numeric control mill (Prototrak DPM SX2). The heat load is provided by two film heaters that are individually controlled by variable transformers (Staco 3PN2110B). Four T-type surface thermocouples are positioned along the channel at equal intervals to monitor the wall temperature. The data are recorded using a National Instrument DAQ NI9213 linked to a customized LABVIEW program. The film heaters and surface thermocouples are inserted between the CPVC and a 3.2 mm thick copper plate in a sandwich configuration. This ensures a good contact between the thermocouples and the film heaters. A thermal compound is applied between the copper plate and the heaters to minimize the contact resistance. The outside walls of the cooling channel are thermally insulated with 2 in. thick polystyrene foam insulation. The thermal test setup is shown

**Table 1   Test equipment and uncertainty of the measurement apparatus**

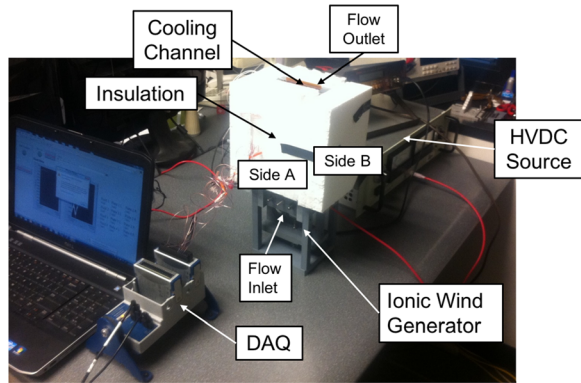| Device | Model | Uncertainty |
|---|---|---|
| Airflow sensor | Degree Controls UAS 2000 | $u > 1$ m/s: $\pm 10\%$ |
| | | $u < 1$ m/s: $\pm 20\%$ |
| Digital ammeter | Fluke 179 | 1.5% + three counts |
| Digital ohmmeter | Fluke 179 | 0.9% + two counts |
| Surface thermocouple | Omega T-type | $\pm 1$ °C |
| Variac | Staco 3PN2110B | N/A |
| 16 Ch. thermocouple DAQ | NI 9213 | N/A |
| Film heaters | Omega KH-304/2, Omega KH-308/2 | N/A |
| High voltage power supply | Spellman CZE1000R | N/A |

**Fig. 3   Experimental setup for the thermal tests**

in Fig. 3. The key parameters defining the ionic wind generator are the electrode spacing $d_1$, the channel width $d_2$, and the applied voltage $\Phi_0$, as shown in Fig. 4.

### Results

Three sets of experimental results are collected and compared to the model prediction. First, the Corona current is characterized experimentally as a function of the channel width and electrode spacing. Second, the velocity is measured at the exit of the ionic wind generator. Third, a thermal test is conducted on a single channel and the average heat flux through the channel wall is reported.

**Corona Current Characterization.** The Corona current is characterized experimentally using the test bench described in the Experimental Setup section. A set of 597 data points were collected at three different voltage levels and covering a large range of electrode spacing ($d_1$) and channel width ($d_2$). A multivariate regression is performed following Chap. 12 in Ref. [12]. The three expressions best describing the Corona current at different voltages are listed in Eqs. (7)–(9) alongside the respective validity
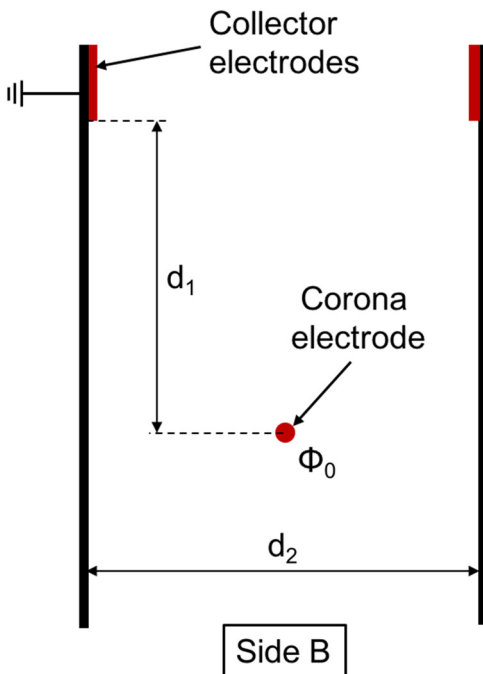


**Fig. 4   Key parameters of the ionic wind generator**

ranges. Thereby, the values of $d_1$ and $d_2$ are in millimeters. The values presented were measured with a Corona electrode length of 80 mm. The value of the Corona current for a wire of a different length can be linearly extrapolated from the presented data, i.e., the magnitude of the Corona current with a wire twice as long will be doubled. The upper bound in $d_1$ is typically constrained by the minimal Corona current requirement. The lower bound in $d_1$ is constrained by the distance at which a full discharge occurs. The distance $d_2$ is bound to 20 mm by the size of the experimental setup, while the lower bound is limited by either a full discharge at low values of $d_1$ or by the minimal Corona current requirement. The present equations are useful in conjunction with the numerical model as it can be used as a design tool for the development of heat sinks using ionic wind

$$I_{\text{Corona},V=10.5} = 179.97 - 31.01d_1 + 4.55d_2 + 1.47d_1^2$$
$$- 0.129d_2^2 - 0.0233d_1^3$$
$$\text{within}$$
$$7.5 \leq d_2 \leq 20 \text{ mm}$$
$$d_1 - d_2 \leq 5 \text{ mm}$$
$$3d_1 - d_2 \geq 35 \text{ mm}$$

(7)

$$I_{\text{Corona},V=13.5} = 305.06 - 41.09d_1 + 2.184d_2 + 1.763d_1^2$$
$$- 0.0254d_1^3 - 0.0022d_1d_2^2$$
$$\text{within}$$
$$12.5 \leq d_1 \leq 25 \text{ mm}$$
$$10 \leq d_2 \leq 20 \text{ mm}$$

(8)

$$I_{\text{Corona},V=16.5} = 444.08 - 57.06d_1 + 3.694d_2 + 2.363d_1^2$$
$$- 0.033d_1^3 - 0.00406d_1d_2^2$$
$$\text{within}$$
$$16 \leq d_1 \leq 25 \text{ mm}$$
$$7.5 \leq d_2 \leq 20 \text{ mm}$$

(9)

**Velocity Measurement.** The air velocity sensor is positioned 1 mm above the channel outlet and 15 mm from the edge of the channel. The airflow sensor is moved across the channel opening, and measurement points are taken every 1.6 mm. The test measurement is performed for three different configurations covering the range of interest for the voltage, the channel width, and the interelectrode spacing. The parameters for the three cases are reported in Table 2. The velocity profile calculated numerically is plotted alongside the experimental measurement points in Figs. 5–7. Due to the high sensitivity of the airflow sensor, the value of the velocity measured tends to slightly vary over time. Therefore, each data point in Figs. 5–7 is averaged over a minimum of ten samples, and a characteristic plot is shown in Fig. 8. Further, a representative plot of the flow pattern is shown in Fig. 9 for a vertical electrode spacing of 15 mm, a channel width of 20 mm, and an applied voltage of 13.5 kV. Typically, the velocity magnitude is much lower in the horizontal direction than in the vertical direction.

**Table 2   Parameters for the three cases of air velocity measurement at the exit of the channel**

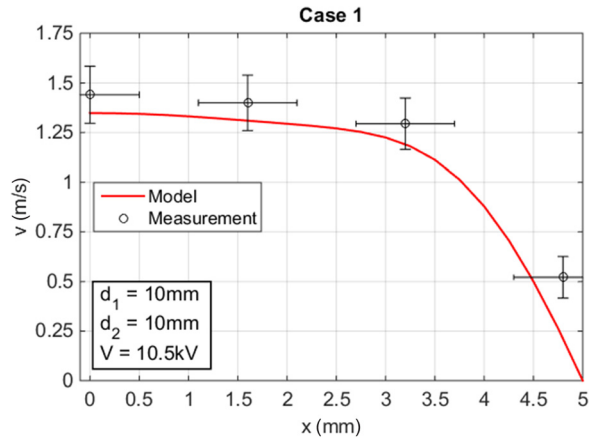| Test no. | Applied voltage, $\Phi_0$ (kV) | Electrode spacing, $d_1$ (mm) | Channel width, $d_2$ (mm) |
|---|---|---|---|
| 1 | 10.5 | 10 | 10 |
| 2 | 13.5 | 15 | 20 |
| 3 | 16.5 | 20 | 15 |

Fig. 5 Comparison of the velocity measurement at the exit of the ionic wind generator with the model prediction for case #1
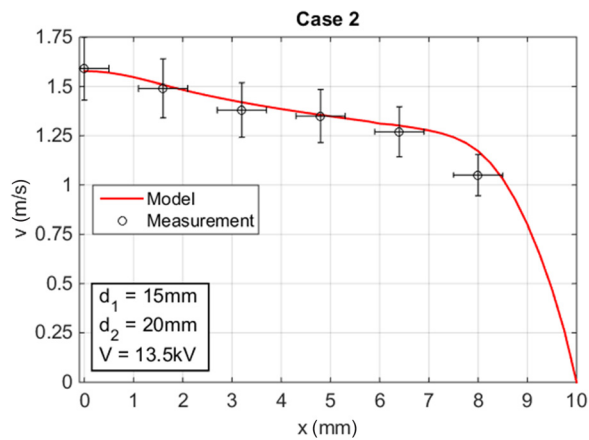


Fig. 6 Comparison of the velocity measurement at the exit of the ionic wind generator with the model prediction for case #2
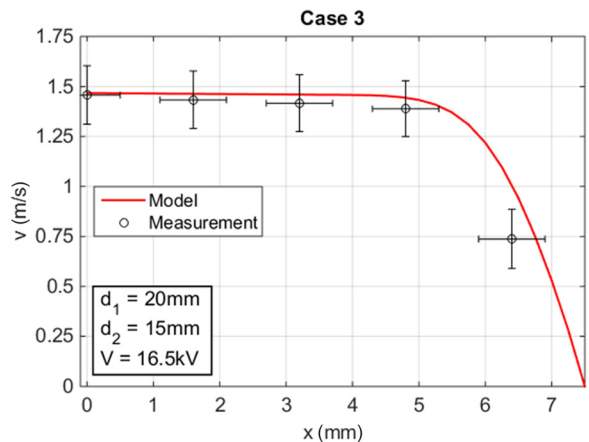


Fig. 7 Comparison of the velocity measurement at the exit of the ionic wind generator with the model prediction for case #3

The velocity measurement shows very good agreement with the model prediction. For all the data points, the model predictions coincide with the velocity measurement within the uncertainty bounds. Therefore, it is shown that the multiphysics numerical model accurately captures the effect of ionic wind flow enhancement in the present configuration of flow between parallel plates.
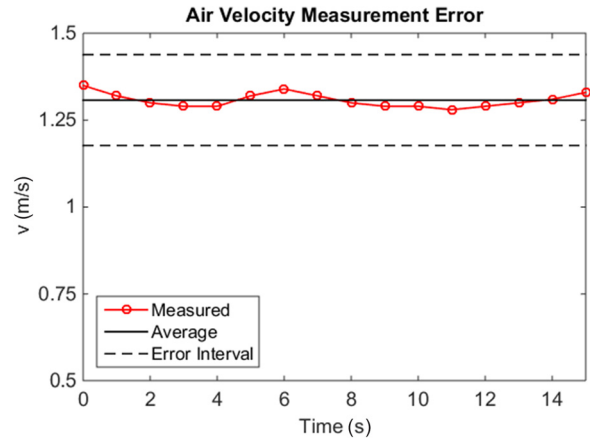


Fig. 8 Measurement sensitivity of the airflow sensor. Each data point is averaged over a minimum of ten samples.

**Thermal Testing.** In order to validate the thermal model, six different tests are conducted. Thereby, the parameters of the ionic wind generator are kept constant at an electrode spacing, a channel width, and a voltage of $d_1 = 15$ mm, $d_2 = 15$ mm, and $\Phi_0 = 13.5$ kV, respectively. Two different cooling channels $L_{HW}$ of length 100 mm and 200 mm are considered. Each of the channel is tested at three different heat loads. The load conditions of the different thermal tests performed are summarized in Table 3. Thereby, the subscripts 1 and 2 arbitrarily denote one side and the other of the channel. It is noticed that the electrical resistance of the film heaters is temperature dependent. Therefore, the values reported were measured once the system had reached thermal steady-state. Thermal steady-state was defined as the situation when the wall temperature change did not exceed 0.1 °C over 10 min.

The transient wall temperatures are plotted in Fig. 10 for the six different thermal tests. Depending on the heat load, thermal steady state was reached within 150–200 min. The wall temperature is close to being uniform, with a maximal temperature difference of 4 °C and 7 °C for the 100 mm and 200 mm channel, respectively. Typically, the entry region of the channel is colder as fresh air is entering the channel. It is noticed that, for the 100 mm channel, the highest temperature $T_{W,3}$ was measured at the location 3 as shown in Fig. 1. This might be due to unequal spreading of the thermal interface leading to slightly different thermal resistances between the thermocouple and the copper plate or to cooling of the channel through the upper edges.

One of the challenges of testing heat sinks with moderate convective heat transfer coefficients is that heat losses that can safely be neglected at higher convective heat transfer coefficients—for instance, when dealing with liquid cooling—have to be accounted for. In the present setup, not all of the power dissipated $P_{Tot}$ is transferred to the fluid flowing through the cooling channel. The different losses are considered separately and subtracted from the total power dissipated $P_{Tot}$ in order to calculate the actual heat flux in the cooling channel. The heat losses can be classified in four categories: heat losses by convection through the sides, through the top, and through the bottom surfaces, as well as radiation from the thermal test setup to the surroundings. The total losses are computed using the equivalent thermal resistance network shown in Fig. 11. Thereby, the convective heat transfer coefficients are calculated using the established Nusselt number correlations [13]. The multidimensional heat conduction effects in the polystyrene insulation layer are considered using conduction shape factors following the method presented by Holman [14]. The total heat transfer surface area consists of the surface of the copper plate in the channel and the surface of the ionic wind generator. The latter is discounted by the corresponding fin efficiency to account for conduction losses along the CPVC structure. The
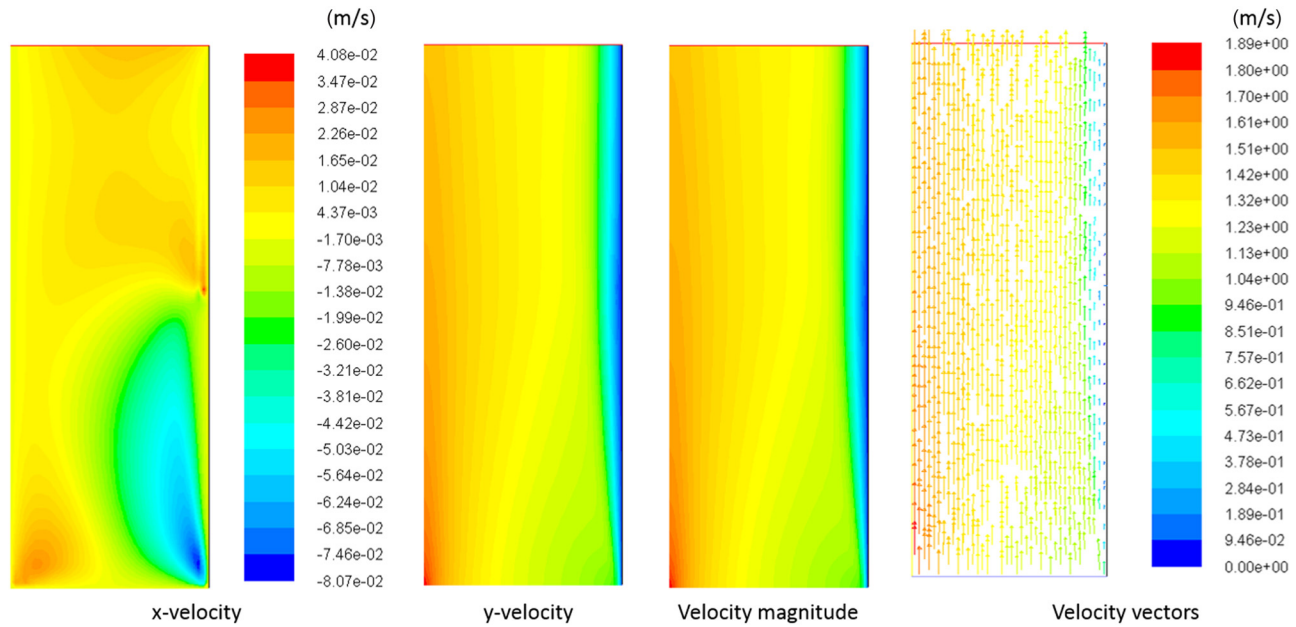
**Fig. 9  Velocity magnitude and vector field at a vertical electrode spacing of $d_1 = 15\,mm$ and a channel width of $d_2 = 20\,mm$**

**Table 3  Power dissipated during the different tests with the corresponding uncertainty**

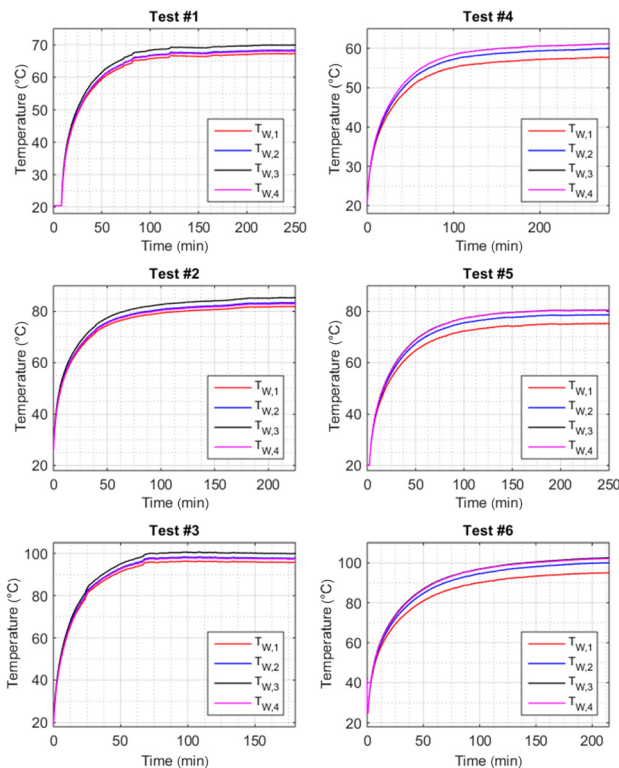| Test no. | Cooling channel length, $L_{HW}$ (mm) | Dissipated power in first wall, $P_1$ (W) | Dissipated power in second wall, $P_2$ (W) | Total power dissipated, $P_{Tot}$ (W) | Total uncertainty in power dissipation, $\sigma_{P_{Tot}}$ (W) |
|---|---|---|---|---|---|
| 1 | 100 | 9.64 | 9.65 | 19.29 | 0.48 |
| 2 | 100 | 13.11 | 12.93 | 26.05 | 0.64 |
| 3 | 100 | 16.48 | 16.33 | 32.81 | 0.80 |
| 4 | 200 | 12.23 | 11.89 | 24.12 | 0.58 |
| 5 | 200 | 17.85 | 17.90 | 35.49 | 0.85 |
| 6 | 200 | 24.71 | 24.86 | 49.57 | 1.17 |



**Fig. 10  Transient wall temperatures for the six thermal tests**

heat dissipated, the total losses, and the net heat flux dissipated in the cooling channel are reported in Table 4.

The thermal model is run for each of the measurement cases presented in Table 3. The walls are set to a known temperature profile along the channel corresponding to the temperature measured during the tests. Thereby, a piecewise constant temperature profile is assumed between the measurement points. This assumption is reasonable as it was observed that the maximal temperature difference between the two measurement points did not exceed 5 °C. In order to account for the uncertainty of the experimental inputs to the model, the simulation is performed three times for
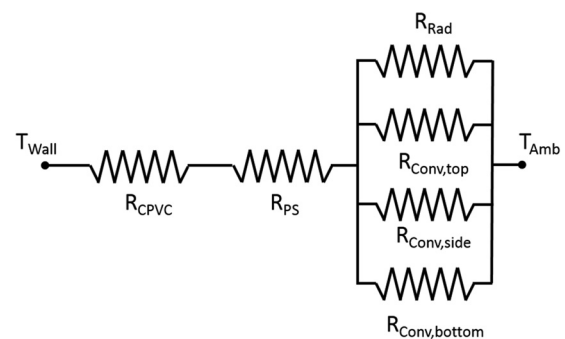


**Fig. 11  Equivalent resistance network to compute the loss through the channel walls and insulation layers. Thereby, RPS stands for the thermal resistance of the polystyrene foam insulation.**

**Table 4 Heat dissipated, net heat transfer rate to the fluid, and the corresponding heat flux through the channel walls**

| Test no. | Heat dissipated, $Q_{\text{Tot}}$ (W) | Parasitic loss, $Q_{\text{Loss}}$ (W) | Net heat, $Q_{\text{Net}}$ (W) | Uncertainty, $\sigma_{Q\text{Net}}$ (W) | Heat transfer area, $A_{\text{HT}}$ (m$^2$) | Net heat flux, $q''$ (W/m$^2$) | Uncertainty, $\sigma_q''$ (W/m$^2$) |
|---|---|---|---|---|---|---|---|
| 1 | 19.28 | 5.24 | 14.04 | 0.62 | 0.021 | 669.7 | 29.4 |
| 2 | 26.04 | 7.17 | 18.87 | 0.76 | 0.021 | 900.3 | 36.1 |
| 3 | 32.81 | 9.25 | 23.56 | 0.90 | 0.021 | 1124.1 | 43.2 |
| 4 | 24.12 | 7.68 | 16.44 | 0.93 | 0.040 | 410.2 | 23.1 |
| 5 | 35.49 | 9.88 | 25.61 | 1.12 | 0.040 | 639.0 | 27.8 |
| 6 | 49.57 | 13.99 | 35.58 | 1.39 | 0.040 | 887.6 | 34.7 |

**Table 5 Comparison of the thermal model with the experimental results**

| Test no. | Predicted heat flux, $q''_{\text{Model}}$ (W/m$^2$) | Measured heat flux, $q''_{\text{Experimental}}$ (W/m$^2$) | Error (%) |
|---|---|---|---|
| 1 | 659.9 | 669.7 | −1.46 |
| 2 | 878.2 | 900.3 | −2.45 |
| 3 | 1090.8 | 1124.1 | −2.96 |
| 4 | 399.6 | 410.2 | −2.59 |
| 5 | 615.6 | 639.0 | −3.66 |
| 6 | 868.5 | 887.6 | −2.16 |
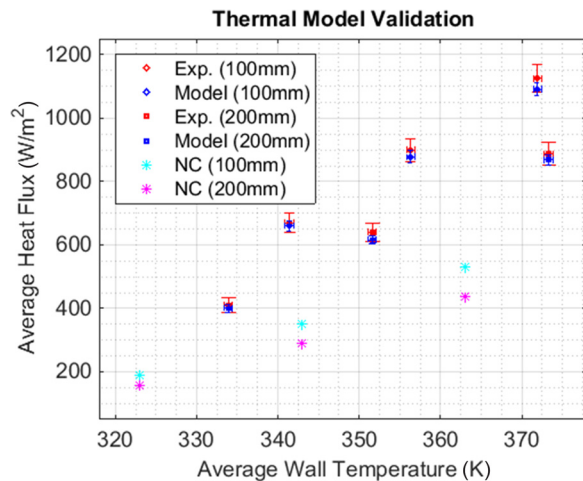


**Fig. 12 Comparison of the model prediction to the experimental data for two cooling channels of length 100 mm and 200 mm**

each test point. There are two sources of uncertainty: the experimental error of the Corona current and the uncertainty of the temperature measurement, which is $\pm 1\,^\circ$C. The first simulation is carried out with the nominal values for the temperature and the Corona current. The second and third simulations are performed considering a lower and upper bound for the average heat flux.

The average heat flux through the channel wall computed by the model is reported and compared to the experimental values in Table 5 and plotted in Fig. 12.

The thermal model shows a very good agreement with the experimental measurements. It is observed that the model consistently slightly underestimates the heat flux measured during the experiments. This effect is probably due to minor heat leakages that are hard to quantify and therefore neglected, such as the conduction through the structure of the test setup. Nevertheless, the present results allow to confirm the validity of the thermal model as all the measurement points fall within the experimental uncertainty bounds.

**Efficiency of the Ionic Wind Generator.** The efficiency of the ionic wind heat transfer enhancement is of interest. A coefficient of performance (COP) is defined as shown in Eq. (10) following the work by Ong et al. [15]. Thereby, $Q_{\text{IW}}$ describes the heat transfer rate with ionic wind enhancement, $Q_{\text{NC}}$ is the heat transfer rate by natural convection only, and $P_{\text{El}}$ is the electrical energy input

$$\text{COP} = \frac{Q_{\text{IW}} - Q_{\text{NC}}}{P_{\text{El}}} \tag{10}$$

The COP is calculated for a set of representative results and is reported in Table 6. It ranges from 9.3 to 22.3. The work performed by Kribs et al. suggests that the ionic wind generator can be more efficient than axial fans [16].

## Technology Demonstrator

The main objective of building a technology demonstrator is to prove the applicability of ionic wind combined with a fin array to the cooling of power electronics, as shown in Fig. 13. The technology demonstrator is designed for the thermal management of a 50 kVA power converter augmented transformer (PCAT). The three converter modules generate up to 80 W each, for a total heat loss of 240 W. The latest thermal management system is composed of a dual-loop thermosiphon using the dielectric medium of the transformer as cooling fluid [17]. A novel heat sink design combining a fin array with ionic wind could potentially replace the current system at a lower cost. This application field is especially attractive for ionic wind as a high voltage source is inherently present in the system.

**Table 6 COP of the presented ionic wind generator for a representative case with a channel width $d_2$ of 15 mm, an interelectrode spacing $d_1$ of 15 mm, and an applied voltage of 13.5 kV**

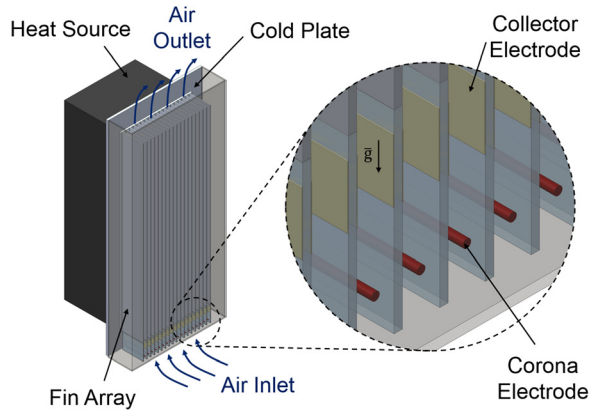| Channel length (mm) | Wall temperature (K) | Average heat flux natural convection (W/m$^2$) | Average heat flux w/ionic wind (W/m$^2$) | COP |
|---|---|---|---|---|
| 100 | 363 | 541.9 | 972.8 | 20.5 |
| | 343 | 362.8 | 678.9 | 15.0 |
| | 323 | 196.4 | 391.2 | 9.3 |
| 200 | 363 | 460.0 | 694.2 | 22.3 |
| | 343 | 307.8 | 482.8 | 16.7 |
| | 323 | 166.5 | 276.4 | 10.5 |

**Fig. 13 Heat sink design combining a fin array and an ionic wind generator**

The heat sink was fabricated in-house. The extruded fin array is made of 6063 aluminum. It was cut to length, and a separate aluminum plate was water-jet cut and attached at the back of the fin array to form closed rectangular channels. The ionic wind generator was made out of two layers of plastic material, each layer being 13 mm thick. The profile of the channel array was water-jet cut. Both layers were assembled and glued together. Holes were drilled for the thin wire electrode to be mounted. A single wire electrode was passed through all the channels. As the fin array is made of aluminum, it was directly grounded and therefore used as the collector electrode. The three copper heater blocks simulating the heat load of the converters were bolted to the cold plate. Thermal paste was applied at the interface to minimize the contact resistance. The heat sink was mounted on an aluminum frame. The high voltage power supply was a Spellman CZE1000R. The temperature of the individual heater blocks was recorded using T-type surface thermocouples. The technology demonstrator along with the test equipment is shown in Fig. 14.

The transient temperature profile under each of the heater block is shown in Fig. 15. At $t = 0$, the system is in equilibrium at ambient temperature. At $t = 2$ min, the heaters are turned on to full power, i.e., three times 80 W. In the first phase of the test, the system is subject to natural convection only, without ionic wind heat transfer enhancement. The current flowing through the heaters was measured to be 2.27 A, and the electrical resistance at thermal steady-state is 46.9 $\Omega$. Therefore, the total power dissipated amounts to $241.7 \pm 8.5$ W. It is noticed that the temperature between each of the heaters differs by up to 6 °C. The reason for this behavior is that the heater blocks were not controlled individually but connected in parallel and supplied with the same
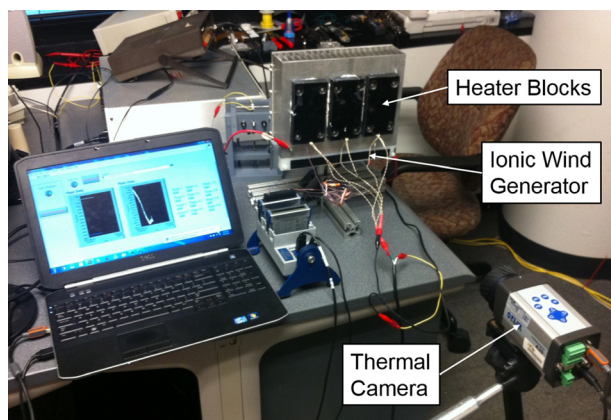


**Fig. 14 Technology demonstrator of ionic wind heat transfer enhancement in conjunction with a fin array**
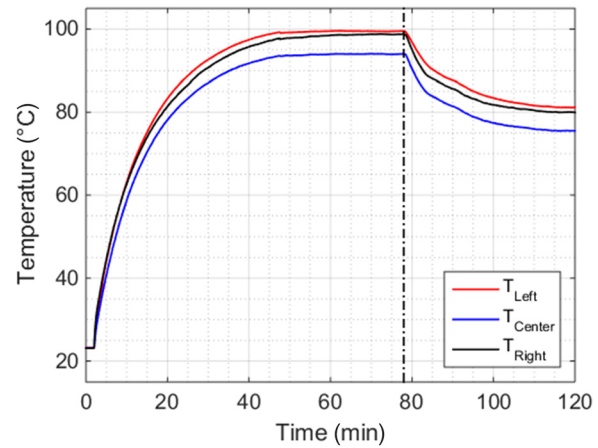


**Fig. 15 Transient temperature profile of the cold plate below each of the heaters. At $t = 2$ min, the heaters were turned on. At $t = 78$ min, the ionic wind generator was turned on, resulting in an immediate decrease of the cold plate temperature.**

voltage. The individual heater blocks might have slightly different electrical resistances, which would result in an inhomogeneous heat generation between the heaters. The system reached thermal steady-state after about 60 min. With natural convection only, the maximal cold plate temperature was 99.5 °C. At $t = 78$ min, the ionic wind generator was turned on, resulting in an immediate decrease of the cold plate temperature. Thermal steady-state for the case with ionic wind heat transfer enhancement was reached after an additional 40 min. In this state, the maximal cold plate temperature was decreased by 18.3–81.2 °C. This is a substantial improvement: a reduction of the operating temperature of 20 °C can result in more than doubling the lifetime of the power electronic components [18].

## Discussion

Measuring low air velocities in tiny spaces is challenging, as the change in dynamic pressure is hardly measurable and pitot tubes therefore not usable. A microhot wire anemometer proved to be a viable alternative. The obtained measurements show a good agreement with the model prediction. It is interesting to notice that in the first case, with a channel width of 10 mm only, the experimental measurement is slightly higher than the model prediction. One possible explanation is that, despite the small size of the velocity sensor, the channel obstruction due to the anemometer slightly increases the air velocity at the measurement point, thus explaining the higher value measured as compared to the velocities calculated using the model. This effect is less pronounced for wider channels. Another interesting observation is that the shape of the velocity profile at the exit of the ionic wind generator changes depending on the configuration. This is explained by the ion concentration distribution in the interelectrode spacing. The distribution of the vertical body force induced through ionic wind is plotted in Fig. 16, and the resulting velocity profile at the exit of the ionic wind generator is shown in Fig. 17. For narrow channels, the ions produced by the Corona electrode reach the wall before they attain the collector electrode and subsequently drift along the wall. This results in a higher ion concentration close to the wall, which in turn leads to a higher body force. Therefore, the velocity profile is distorted and a maximum occurs somewhere between the center of the channel and the wall. This effect is less important for wider channels and the dominant body force is close to the Corona electrode, resulting in a maximal velocity in the center of the channel. Note that the velocity profile shown in Fig. 5 does not have the same shape as the first plot in Fig. 17. This is due to the applied lower profile.
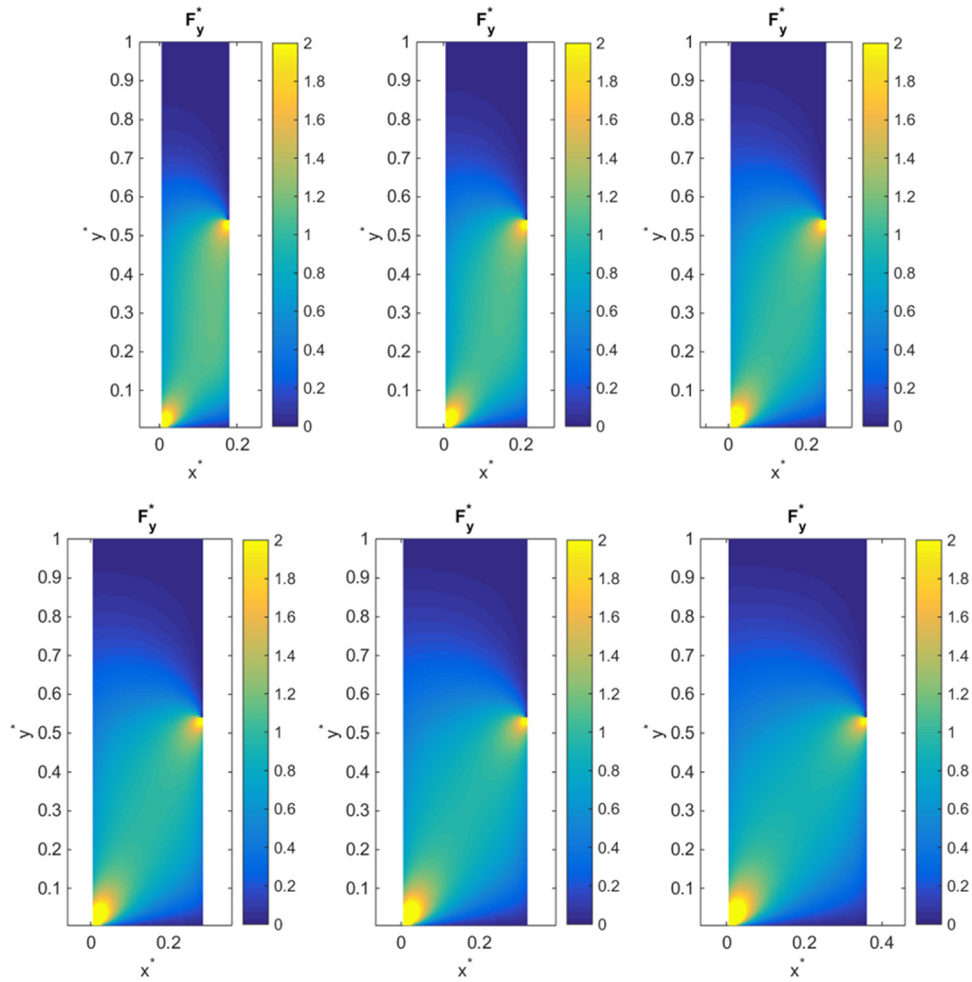
**Fig. 16  Vertical body force induced by ionic wind at an electrode spacing of 15 mm and an applied voltage of 13.5 kV for different channels' widths (from top left to bottom right: 10 mm, 12 mm, 14 mm, 16 mm, 18 mm, and 20 mm)**
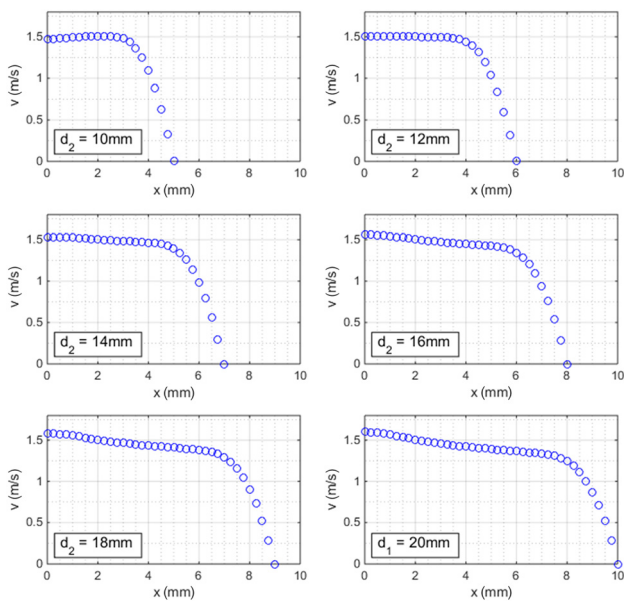


**Fig. 17  Induced velocity profile depending on the channel width, all other parameters are kept constant**

The thermal testing also brought about challenges. Even though the single channel used for the thermal test was insulated with 2 in. thick polystyrene foam, thermal losses through the walls and by radiation have to be accounted for. Indeed, because the convective heat transfer coefficients expected in the channel are moderate—in the order of 10–20 W/m$^2$ K—the heat losses across the insulation and through radiation have a significant impact on the measurements. Further, because the heat dissipation is relatively low, steady-state was not reached before several hours. Nevertheless, the multiphysics model developed in the previous chapter could be validated, and all the model predictions fall within the measurement uncertainty of the experimental data points.

## Conclusion

The multiphysics numerical model of ionic wind heat transfer enhancement developed in the previous work was validated experimentally. The validation was performed at two levels: first, the velocity profile was measured at the exit of the ionic wind generator. Second, the heat flux dissipated in the cooling channel was measured and compared to the value predicted by the numerical prediction. It is shown that the model correctly captures the effect of ionic wind heat transfer enhancement, and all the model predictions fall within the measurement uncertainty of the experimental data points. Finally, the applicability of the proposed concept combining a fin array with an ionic wind generator was demonstrated by building a prototype of a heat sink for an existing

PCAT. The effect of ionic wind is clearly noticeable, as the cold plate temperature is reduced by over $18\,^{\circ}\mathrm{C}$ as compared to the case with natural convection only. Further, relying on ionic wind rather than pure natural convection offers more freedom in the design of the heat sink, as there is no requirement for minimal height difference or channel orientation to maintain an air flow through the channel. Therefore, it is demonstrated that ionic wind is a viable technology to increase the cooling power of a heat sink.

## Acknowledgment

## Nomenclature

$A_{\mathrm{HT}}$ = heat transfer surface area (m$^2$)
$b$ = ion mobility in air (m$^2$/V s)
$c_p$ = specific heat of air (J/kg K)
$d_1$ = vertical spacing between Corona electrode and collector electrode (mm)
$d_2$ = heat exchanger channel width (mm)
$D_{\mathrm{IA}}$ = ion diffusion coefficient in air (m$^2$/s)
$e$ = elemental charge (C)
$E$ = electric field (V/m)
$k$ = thermal conductivity of air (W/m K)
$L_{\mathrm{HW}}$ = length of the heated channel (m)
$n_e$ = concentration of free electrons (1/m$^3$)
$n_+$ = concentration of positive ions (1/m$^3$)
$n_-$ = concentration of negative ions (1/m$^3$)
$P$ = electrical power dissipated in film heaters (W)
$Q$ = heat transfer rate (W)
$q''$ = heat flux (W/m$^2$)
$T$ = air temperature (K)
$u$ = horizontal velocity magnitude (m/s)
$v$ = vertical velocity magnitude (m/s)
$\varepsilon$ = air permittivity (F/m)
$\nu$ = kinematic viscosity (m$^2$/s)
$\rho$ = air density (kg/m$^3$)
$\rho_e$ = free charge density (1/m$^3$)
$\sigma$ = electrical conductivity of air (1/$\Omega$ m)
$\sigma_X$ = experimental uncertainty of variable $X$
$\Phi$ = potential (V)

## References

[1] Steinke, M. E., 2012, *Contemporary Perspectives on Air Cooling of Electronic Components*, Begell House Publishers, Danbury, CT.
[2] Hsu, C. P., Sticht, C., Jewell-Larsen, N. E., Fox, M., Krichtafovitch, I. A., and Mamishev, A. V., 2008, "Characterization of Microfabricated Cantilever-to-Plane Electrostatic Fluid Accelerators for Cooling in Electronics," ASME Paper No. IMECE2007-42104.
[3] Go, D. B., Maturana, R. A., Fisher, T. S., and Garimella, S. V., 2008, "Enhancement of External Forced Convection by Ionic Wind," Int. J. Heat Mass Transfer, **51**(25–26), pp. 6047–6053.
[4] Go, D. B., Fisher, T. S., and Garimella, S. V., 2006, "Direct Simulation Monte Carlo Analysis of Microscale Field Emission and Ionization of Atmospheric Air," ASME Paper No. IMECE2006-14476.
[5] Wang, P., Fan, F.-G., Zirilli, F., and Chen, J., 2012, "A Hybrid Model to Predict Electron and Ion Distributions in Entire Interelectrode Space of a Negative Corona Discharge," IEEE Trans. Plasma Sci., **40**(2), pp. 421–428.
[6] Cagnoni, D., Agostini, F., Christen, T., Parolini, N., Stevanovic, I., and de Falco, C., 2013, "Multiphysics Simulation of Corona Discharge Induced Ionic Wind," J. Appl. Phys., **114**(23), p. 233301.
[7] Gallandat, N., and Mayor, J. R., 2015, "Novel Heat Sink Design Utilizing Ionic Wind for Efficient Passive Thermal Management of Grid-Scale Power Routers," ASME J. Therm. Sci. Eng. Appl., **7**(3), p. 031004.
[8] Gallandat, N., and Mayor, J. R., 2015, "Errata to the Paper Novel Heat Sink Design Utilizing Ionic Wind for Efficient Passive Thermal Management of Grid-Scale Power Routers," ASME J. Therm. Sci. Eng. Appl., **7**(3), p. 031004.
[9] Junhong, C., and Davidson, J. H., 2002, "Electron Density and Energy Distributions in the Positive DC Corona: Interpretation for Corona-Enhanced Chemical Reactions," Plasma Chem. Plasma Process., **22**(2), pp. 199–224.
[10] Stuetzer, O. M., 1959, "Ion Drag Pressure Generation," J. Appl. Phys., **30**(7), pp. 984–994.
[11] Owsenek, B. L., and Seyed-Yagoobi, J., 1997, "Theoretical and Experimental Study of Electrohydrodynamic Heat Transfer Enhancement Through Wire-Plate Corona Discharge," ASME J. Heat Transfer, **119**(3), pp. 604–610.
[12] Barnes, J. W., 1994, *Statistical Analysis for Engineers and Scientists: A Computer-Based Approach*, McGraw-Hill, New York.
[13] Incropera, F. P., 2007, *Fundamentals of Heat and Mass Transfer*, Wiley, New York.
[14] Holman, J. P., 1990, *Heat Transfer*, 7th ed., McGraw-Hill, New York.
[15] Ong, A. O., Abramson, A. R., and Tien, N. C., 2014, "Electrohydrodynamic Microfabricated Ionic Wind Pumps for Thermal Management Applications," ASME J. Heat Transfer, **136**(6), p. 061703.
[16] June, M. S., Kribs, J., and Lyons, K. M., 2014, "Integrated Ionic Flow Device and Heat Sink as a Fan Sink Alternative," Proceedings of the ESA Annual Meeting on Electrostatics, Notre Dame, IN, June 17–19.
[17] Hesse, D. L., Mayor, J. R., and Semidey, S. A., 2014, "Analytical Modeling of Dual-Loop Single Phase Thermosiphons for Power Electronics Cooling," ASME Paper No. IMECE2014-38718.
[18] Schulz, M., 2011, "Thermal Interface–A Key Factor in Improving Lifetime in Power Electronics," International Exhibition and Conference for Power Electronics, Intelligent Motion and Power Quality, Nuremburg, Germany, May 8–10, pp. 1317–1321.